

# Magnetically Enhanced Microflow Cytometer for Bead-based Immunoaffinity Measurements in Whole Blood Samples



Scientific thesis for the attainment of the academic degree  
Master of Science (M.Sc.)  
of the Department of Electrical and Computer Engineering  
at the Technical University of Munich.

**Supervised by** Dr.-Ing. Mathias Reisbeck  
Prof. Dr. rer. nat. Oliver Hayden

**Submitted by** Johann Alexander Brenner  
Weisbergerstraße 5a  
85053 Ingolstadt  
03662733

**Submitted on** December 4<sup>th</sup>, 2020 at Munich





# Contents

<b>List of Abbreviations .....</b>	<b>0</b>
<b>1 Theory .....</b>	<b>1</b>
1.1 Microfluidics .....	1
1.1.1 Incompressibility of Fluid Flows .....	1
1.1.2 Flow and Shear in Microchannels with Viscous Fluids .....	2
1.1.3 Force Equilibrium of Microbeads .....	4
1.1.4 Rolling Motion and Surface Interaction of Beads.....	10
1.2 Surface Chemistry .....	15
1.2.1 Surface Oxidation Methods.....	15
1.2.2 Silane Chemistry .....	18
1.2.3 Carbodiimide Crosslinker Chemistry .....	19
1.2.4 The Biotin-Avidin-System .....	22
1.3 Magnetoresistive Sensing .....	23





# List of Abbreviations

## Symbols

$Q$ - flow rate.....
$\chi$ - magnetic susceptibility.....
$\eta$ - dynamic viscosity.....
$\omega$ - angular rotation frequency .....
$\tau$ - surface stress tensor.....
$\tau_{\text{pressure}}$ - pressure stress tensor.....
$\tau_{\text{viscous}}$ - viscous stress tensor.....
$\varepsilon$ - shear stress tensor .....
$\mathbf{B}$ - magnetic flux density.....
$\mathbf{F}_{\text{buoyancy}}$ - buoyancy .....
$\mathbf{F}_{\text{drag}}$ - Stoke's drag force.....
$\mathbf{F}_{\text{el}}$ - Coulomb's force .....
$\mathbf{F}_{\text{grav}}$ - gravity .....
$\mathbf{F}_{\text{magnus}}$ - Magnus lift force .....
$\mathbf{F}_{\text{mag}}$ - magnetic force .....
$\mathbf{F}_{\text{saffman}}$ - Saffman lift force.....
$\mathbf{F}_{\text{shear}}$ - shear-induced lift force.....
$\mathbf{M}$ - magnetization.....
$T_{\text{crit}}$ - critical tension.....
$\Omega$ - rotation vector .....
$\mathbf{m}$ - magnetic dipole moment .....
$\mathbf{u}$ - flow field.....
$\mathbf{u}_s$ - sedimentation velocity.....
$Re_{\text{particle}}$ - particle Reynolds number .....
$Re$ - Reynolds number .....
$\vec{n}$ - unit outward normal .....
$\rho$ - density .....

## A

amine - $-\text{NH}_2$ .....
APTES - 3-triethoxysilylpropan-1-amine .....

**C**

carboxamide - R<sub>1</sub>-CONH-R<sub>2</sub>.....  
carboxyl - -COOH .....

**E**

EDC - 3-(Ethyliminomethyleneamino)-N,N-dimethylpropan-1-amine.....  
ethoxy - -O-CH<sub>2</sub>-CH<sub>3</sub>.....

**G**

GMR - giant magneto resistance .....

**H**

H<sub>2</sub>O<sub>2</sub> - hydrogen peroxide .....

H<sub>2</sub>SO<sub>4</sub>4 - sulfuric acid.....

H<sub>2</sub>SO<sub>5</sub> - Caro's acid.....

HF - hydrofluoric acid.....

hydroxyl - -OH .....

**K**

K<sub>d</sub> - dissociation constant.....

**M**

methylene - -CH<sub>2</sub>-.....

**N**

NHS - 1-Hydroxy-2,5-pyrrolidinedione .....

NSE - Navier-Stokes-Equation .....

**O**

O<sub>2</sub> - oxygen gas .....

**P**

PCB - printed circuit board.....

PDMS - poly(dimethylsiloxane).....

piranha - a mixture from hydrogen peroxide with excess of sulfuric acid.....

**R**

RBC - red blood cell.....

## S

SAM - self-assembled monolayer .....

$\text{Si}_3\text{N}_4$  - silicon nitride.....

silanol - Si-OH.....

siloxane - Si-O-Si .....

SNR - signal-to-noise ratio.....

sulfo-NHS - 1-hydroxy-2,5-dioxopyrrolidine-3-sulfonate .....

## Z

z - approach .....



# 1. Theory

The main measurement principle of a microfluidic channel in connection with a giant magneto resistance (GMR)-Sensor has been already described and characterized exhaustively by Helou [1], Reisbeck [2] and others.[3, 4] Therefore, this theoretical part will focus on (bio-)physical aspects of a cell rolling motion inside a microfluidic channel and surface modification chemistry.

## 1.1. Microfluidics

### 1.1.1. Incompressibility of Fluid Flows

The main experiments of this work were carried out in microfluidic environments, which exhibit favorable properties compared to common macrofluidic systems. From a fluid-mechanical perspective, shrinking the scales makes interfacial as well as electrokinetic phenomena much more significant, and reduces the importance of pressure and gravity.[5] However, electrodynamics, chemistry and fluid dynamics are inextricably intertwined, so that fluid flow can create electric fields (and vice versa), with a degree of coupling driven by the surface chemistry. Many of the resulting phenomena arise or can be explained by the conservation of mass described by the continuity equation (Eq. 1.1), the conservation of momentum described by the Cauchy-Momentum equation (Eq. 1.4), and the resulting Navier-Stokes equation (Eq. 1.8).<sup>1</sup>

$$\frac{\partial}{\partial t} \iiint \rho \, dV = - \iint \rho \mathbf{u} \cdot \vec{n} \, dA \quad 1.1$$

$$\nabla \cdot \mathbf{u} = 0 \quad 1.2$$

$$\frac{\partial}{\partial t} \iiint \rho \mathbf{u} \, dV = - \iint \rho \mathbf{u} \mathbf{u} \cdot \vec{n} \, dA + \iint \boldsymbol{\tau} \cdot \vec{n} \, dA + \iiint \sum_i \mathbf{f}_i \, dV \quad 1.3$$

$$\rho \frac{\partial \mathbf{u}}{\partial t} + \rho \mathbf{u} \cdot \nabla \mathbf{u} = \nabla \cdot \boldsymbol{\tau} + \sum_i \mathbf{f}_i \quad 1.4$$

$$1.5$$

---

<sup>1</sup> The mathematical prerequisites and notation for all following derivations are explained in ??

The foremost assumption in fluid dynamics is termed “incompressibility”, when density gradients are negligibly small to assume a uniformity thereof. This leads to a significant simplification of the conservation equations, because any transfer from kinetic to internal energy can be ignored.<sup>2</sup> This equation states that the mass of a control volume - in this case the volume integral over the density ( $\rho$ ) - can only change by the mass flux over its unit outward normal ( $\vec{n}$ ) transported by the flow field ( $\mathbf{u}$ ). For constant  $\rho$  the mass does never change over time. This finding and the application of Gauss's theorem yields the conservation of mass in an incompressible fluid. (Eq. 1.2)

### 1.1.2. Flow and Shear in Microchannels with Viscous Fluids

The final equation and Gauss's theorem can now be applied to the conservation of momentum relation. (Eq. 1.3) Integration yields then the Cauchy momentum equation which states that any change in momentum inside a control volume ( $\rho \frac{\partial \mathbf{u}}{\partial t}$ ) is caused by convective transport for or to the volume ( $\rho \mathbf{u} \cdot \nabla \mathbf{u}$ ), surface stresses ( $\nabla \cdot \boldsymbol{\tau}$ ), and the volumetric net body forces ( $\mathbf{f}_i$ ) such as gravity or electrostatics.

Hereby, the surface stress surface stress tensor ( $\boldsymbol{\tau}$ ) can be further decomposed into the pressure stress tensor ( $\boldsymbol{\tau}_{\text{pressure}}$ ) and viscous stress tensor ( $\boldsymbol{\tau}_{\text{viscous}}$ ) as shown in the equations Eq. 1.6. Characteristically, the pressure related contributions act normal and independently from  $\mathbf{u}$  whereas viscous forces act normal and tangential, and are dependent on  $\mathbf{u}$ . The  $\boldsymbol{\tau}_{\text{pressure}}$  can therefore be expressed by a scalar pressure acting in every spatial dimension which is spanned by the identity.

The viscous stresses however can not be described by a continuum equation but only by a constitutive relation of atomistic processes. The underlying fundamental model of Newton's mechanics assumes that dynamic viscosity ( $\eta$ ) is neither dependent on any velocity nor on the strain rate. Therefor, fluids which satisfy this condition are called “Newtonian fluids”. Omitting special cases such as shear-thinning, -thickening or complex colloidal fluids such as undilute blood,  $\eta$  is the scalar proportionality that relates the strain rate to surface stress.[5] This is captured in the equation  $\boldsymbol{\tau}_{\text{viscous}} = 2\eta\boldsymbol{\epsilon}$ . Thereby, the shear stress tensor ( $\boldsymbol{\epsilon}$ ) is part of the decomposition of an unidirectional flow field. It resembles on the one hand side any stretching or squeezing of fluid by *extensional*

---

<sup>2</sup> For sake of completeness, it should be mentioned that viscous forces can also transfer energy irreversibly to internal energy. However, they are inversely proportional to the system's size, and hence omitted.

*strain* and on the other hand side *shear strain* which is responsible for skewing.[5]

$$\boldsymbol{\tau} = \boldsymbol{\tau}_{viscous} + \boldsymbol{\tau}_{pressure} = 2\eta\boldsymbol{\epsilon} - p\mathbf{I}_{3\times 3} \quad 1.6$$

$$\nabla \cdot \boldsymbol{\tau}_{viscous} = \nabla \cdot 2\eta\boldsymbol{\epsilon} = \nabla \cdot \eta\nabla\mathbf{u} \stackrel{\text{only if } \eta \text{ uniform}}{=} \eta\nabla^2\mathbf{u} \quad 1.7$$

$$\underbrace{\rho \frac{\partial \mathbf{u}}{\partial t}}_{\text{Transient}} + \underbrace{\rho \mathbf{u} \cdot \nabla \mathbf{u}}_{\text{Convection}} + \underbrace{-\nabla p}_{\text{Pressure}} + \underbrace{\eta \nabla^2 \mathbf{u}}_{\text{Viscous}} + \underbrace{\sum_i \mathbf{f}_i}_{\text{Body Forces}} = 0 \quad 1.8$$

The divergence of  $\boldsymbol{\tau}_{viscous}$ , as used in the incompressible Cauchy momentum equation (Eq. 1.4), can then be simplified with Eq. 1.7 further by taking advantage of the anti-transpose symmetry of the flow field. If  $\eta$  is also uniform respectively isotropic across the channel, the divergence is completely independent of the scalar viscosity. Applying all assumptions to the Cauchy momentum equation (Eq. 1.4) yields as final result the Navier-Stokes-Equation (NSE). (Eq. 1.8)

However, the NSE has no analytic solution yet and can in consequence only solve defined boundary problems. The two most common boundary conditions herefore are the “no-penetration condition” ( $\mathbf{u} \cdot \vec{n} = 0$ ) and the “no-slip condition” ( $\mathbf{u}_t = \mathbf{u} - (\mathbf{u} \cdot \vec{n}) \vec{n} = 0$ ), which state that the normal and tangential components of fluid velocity are per definition zero at motionless, impermeable walls.

Besides these conditions, many problems arise due to turbulent flow and therefor transient effects. Mathematically, this can be avoided by simply neglecting the time-dependent term in the NSE. Also, it can be argued from a systematic point of view that, for viscosity-dominated flows, fluid moves in isoplanar “lamina”. In experimental observations, these laminar flows then proved to be steady to perturbations.

$$Re = \frac{\text{fluid density} \cdot \text{velocity} \cdot \text{size}}{\text{viscosity}} \quad 1.9$$

In a first order approximation, the dimensionless Reynolds number ( $Re$ ), which compares the inertia to viscous forces, allows a qualitative prognosis about the flow regime. (Eq. 1.9) If it results below a threshold of 2300, laminar flow can be assumed in Hagen-Poiseuille flows. This holds true for the utilized microfluidic with the dimensions 15 800  $\mu\text{m}$   $\times$  700  $\mu\text{m}$   $\times$  150  $\mu\text{m}$  ( $l \times w \times h$ ) and aqueous buffer solutions, where the channel width considered as *characteristic size*. Hence, several fluidic phenomena such as deter-

ministic pathlines as well as simplifications of the NSE can be exploited in the present system.

In the model case of a flow through a rectangular channel, no analytical solution of the NSE exists, but a Fourier Series expansion if the width is larger than height of a channel as shown in Bruus [6]. Equation Eq. 1.10 determines the magnitude of the flow field parallel to the pressure gradient in relation to the horizontal dimension  $y$  and vertical dimension  $z$  with respect to the channel dimensions height  $h$  and width  $w$ . An integration over the flow field in the channel cross section yields the flow rate ( $Q$ ). (Eq. 1.11)<sup>3</sup>

$$\mathbf{u}_x(y, z) = \frac{4h^2\Delta p}{\pi^3\eta l} \sum_{n, odd}^{\infty} \frac{1}{n^3} \left( 1 - \frac{\cosh(n\pi\frac{y}{h})}{\cosh(n\pi\frac{w}{2h})} \right) \sin(n\pi\frac{z}{h}) \quad 1.10$$

$$Q = \int_{-\frac{1}{2}w}^{\frac{1}{2}w} \int_0^h u_x(y, z) dz dy \approx \frac{h^3 w \Delta p}{12\eta l} \left( 1 - \frac{h}{w} \right), \text{ for } h < w \quad 1.11$$

### 1.1.3. Force Equilibrium of Microbeads

Although microfluidic systems mostly operate in a low inertia regimes as specified by low  $Re$ , the force equilibrium  $\sum_i \mathbf{F} = 0$  and subsequently the velocity of any particle in the fluid stream is influenced as it moves closer to the boundaries. Several models have already been implemented with a part of the mentioned forces. Lee and Balachandar [7] compared the importance of translation, rotation and shear forces. Dong and Lei [8] evaluated cell rolling characteristics, and Wu and Voldman [9] proposed a model for bead-based immunoassays in microfluidics. Therefore, an overview over all (inter-)acting forces shall be given here.

$$Re_{particle} = \frac{r^2}{\frac{2wh}{w+h}} Re \quad 1.12$$

Additionally to the channel Reynolds number  $Re$ , describing the ratio between inertial force and viscous force of fluid in a flow, Di Carlo et al. [10] proposed a particle Reynolds number ( $Re_{particle}$ ) considering the size ratio of particle to channel. At  $Re_{particle} \ll 1$ ,

---

<sup>3</sup> The equation Eq. 1.10 shows that height deviations can have prominent influence on a channel velocity simulation as it is proportional to  $h^2$ . Further, the flow rate depends even on  $h^3$ .

particles are subjected to the dominant viscous drag to follow fluid streamlines. In the contradictory case, inertia becomes prominent. However, on increasing  $Re_{\text{particle}}$  to the order of 1, inertial lift forces become dominant and lateral migration of particles across streamlines becomes visible. For a micrometer sized bead and a channel as referred to in Sec. 1.1.2, the pre-factor is in the range of  $1 \times 10^{-5}$  to  $1 \times 10^{-7}$  hence viscous drag overweighs inertial lift of a particle.

### Stoke's Drag

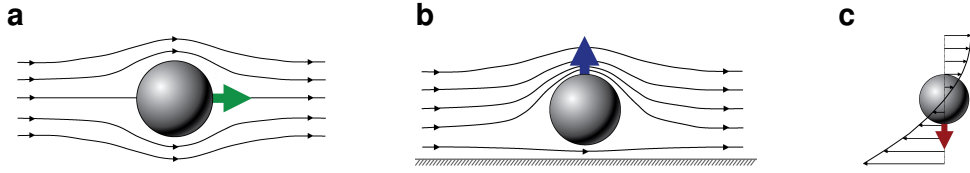


**Figure 1: Particle Drag and Lift Behavior**

(a) Bulk Drag: Force acts on a particle caused by the displacement of fluid stream lines. (b) Wall-lift Drag Force: In a special case of drag, where streamlines cannot be displaced further, a pressure gradient forms in front of the sphere. This forces a motion directed perpendicularly from the wall. (c) Shear-induced force: The curvature of the flow profile exhibits a translation and rotation due to inhomogeneously distributed shear on the surface.[11]

The foremost force to actuate particles inside a microfluidic channel is Stoke's drag force ( $\mathbf{F}_{\text{drag}}$ ). (Eq. 1.13) It originates from viscous fluid moving past the sphere surface, where a slip condition has to be applied. The fluid therefor has to displace its elements in front of the movement direction.[12] A particle with the surrounding streamlines is depicted in Fig. 1a for the bulk case and in Fig. 1c for adjacent walls.

$$\mathbf{F}_{\text{drag},\text{wall}} = -6\pi\eta r \bar{\mathbf{u}} K \quad 1.13$$

$$K = \frac{4}{3} \sinh \alpha \sum_{n=0}^{\infty} \left( \frac{n(n+1)}{(2n-1)(2n+3)} \cdot A \right) \quad 1.14$$

$$\alpha = \cosh^{-1} \frac{z}{r}, \quad 1.15$$

$$A = \frac{2 \sinh((2n+1)\alpha) + (2n+1) \sinh 2\alpha}{(2 \sinh((n+0.5)\alpha))^2 - ((2n+1) \sinh \alpha)^2} - 1 \quad 1.16$$

$$K_{\text{approx}} = \frac{24}{Re} * \left( \frac{1 + \frac{2}{3}\lambda}{1 + \lambda} \right), \text{ with } \lambda = \frac{\eta_{\text{fluid}}}{\eta_{\text{particle}}} \quad 1.17$$

$$v_z = \frac{3}{64} Re_s \mathbf{u}_s = \frac{3}{64} \frac{\rho_{\text{fluid}} r \mathbf{u}_s}{\eta} \mathbf{u}_s, \left( \frac{\rho_{\text{fluid}} l_w \mathbf{u}_s}{\eta} \right) \ll 1 \quad 1.18$$

$$\omega = \frac{3\mathbf{u}}{32r} \left( \frac{r}{l} \right)^4 \left( 1 - \frac{3}{8} \frac{r}{l} \right), \text{ for } \left( \frac{r}{l} \right)^2 \ll 1 \quad 1.19$$

In the proximity of a channel wall, where no fluid can be displaced further, a correction factor was determined by Happel and Brenner [13] that approximates drag in a perpendicular direction.(Eq. 1.14) Repulsion velocity can then be defined by the Reynolds number calculated with a sedimentation velocity ( $u_s$ ) if the particle center has a distance  $l_w \ll 1$  from the wall.[14, 15] A phenomenological approximation of the correction factor yields equation Eq. 1.17, when viscosity dominates the difference. Adapted to an example, a spherical air-bubble inside a water flow feels only 67.4 % of the drag by surrounding fluid.

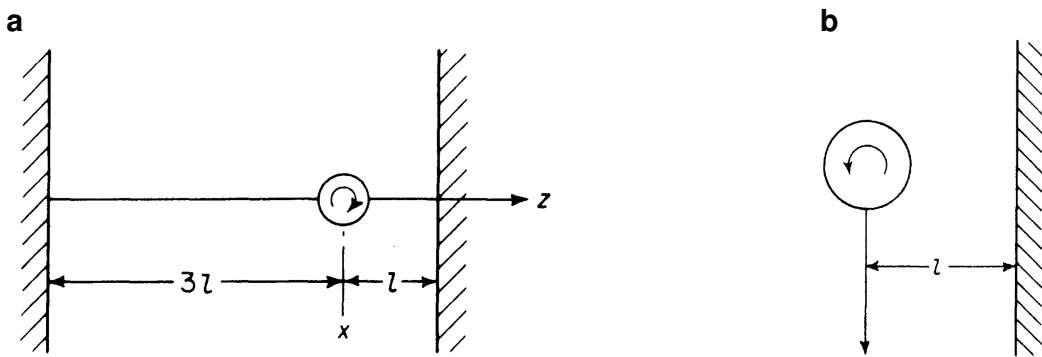


**Figure 2: Particle Rotation Behavior**

(a) Direction of rotation of a sphere settling in eccentric position between parallel walls. (b) Direction of rotation of a sphere settling in the presence of a single plane wall far from the other side.[10]

The considerations of Stoke's drag force above were limited for only linear translation cases. However, fluid drag also imposes a non-negligibly torque on particles if a particle moves nearer than 10 diameters to the wall. Happel and Brenner [13] mention an experimentally determined formula in 1.19 to calculate a drag-related angular rotation frequency ( $\omega$ ). Counter-intuitively, the direction of rotation in the bulk fluid (Fig. 2a) is opposite than from the rotation direction near or touching the wall (Fig. 2c). This can be explained by a complex superposition of tangential components from later mentioned forces and will not be explained to any more extent here.

### Gravity and Buoyancy

On every mass in our environment acts gravity ( $\mathbf{F}_{\text{grav}}$ ) to pull it along its gradient. In a medium, notwithstanding, it is balanced by the displacement of the same in the counter-direction called buoyancy ( $\mathbf{F}_{\text{buoyancy}}$ ). As a microparticle made from a co-polymer - especially when it carries magnetic momentum - has a significantly higher density than water,  $\mathbf{F}_{\text{grav}}$  (Eq. 1.21) outperforms  $\mathbf{F}_{\text{buoyancy}}$  (Eq. 1.20), which in term causes a particle

to sink to the channel floor.

$$\mathbf{F}_{buoyancy} = -\frac{4}{3}\pi r^3 \rho_{fluid} g \quad 1.20$$

$$\mathbf{F}_{gravity} = +\frac{4}{3}\pi r^3 \rho_{particle} g \quad 1.21$$

### Magnetic Force

The - during the course of this thesis - strongest acting force is exhibited by the magnetic flux density ( $\mathbf{B}$ ), which acts on paramagnetic particles with a magnetic dipole moment ( $\mathbf{m}$ ). When an external magnetic field is non-uniform, there will be a magnetic force ( $\mathbf{F}_{mag}$ ), proportional to the magnetic field gradient, acting on the magnetic dipole moment.(Eq. 1.24) For particles that carry magnetite or similar ferrimagnetic material in their polymer shell, the magnetic momentum can be inferred by the relation  $\mathbf{m} = MV$  if the magnetization ( $\mathbf{M}$ ) of a volume  $V$  is known. However, the more exact approach is a comparison of magnetic susceptibilities ( $\chi$ ) as described in Eq. 1.22. Consequently, if the particle susceptibility is greater than the fluid's, a microbead will move towards the field maximum. Calculated for an  $8 \mu\text{m}$  bead with  $1.12 \times 10^{-12} \text{ A m}^2$  saturation magnetization,  $\mathbf{F}_{mag}$  results in  $\sim 45 \text{ pN}$  for a field gradient of  $5 \text{ T m}^{-1}$ .

$$\mathbf{F}_{mag} = \frac{V_p (\chi_p - \chi_f)}{\mu_0} (\mathbf{B} \cdot \nabla) \mathbf{B} \quad 1.22$$

$$\mathbf{F}_{dipole} = (\mathbf{m} \cdot \nabla) \mathbf{B} = -\nabla \mathbf{E}_{dipole} \quad 1.23$$

$$\mathbf{E}_{dipole} = \sum_{i=1}^n \frac{\mu_0}{4\pi r_i^3} \left( \mathbf{m}_i \cdot \mathbf{m}_{ref} - \frac{3}{|\mathbf{r}_i|^2} (\mathbf{r}_i \cdot \mathbf{m}_i) (\mathbf{r}_i \cdot \mathbf{m}_{ref}) \right) \quad 1.24$$

Additionally, the magnetic beads interact with each other according to the dipolar interaction. In that case, a reference bead with magnetic momentum  $\mathbf{m}_{ref}$  at distance  $\mathbf{r}_{ref}$  feels the force of all surrounding particles. (Eq. 1.24)

### Electrostatic Interaction

The microchannel - as well as a particle in it - carries an electrical double layer on the surface due to present surface charges. The net charge acquired by the particles can be computed by integrating the particles' surface charge densities over their surfaces as described by Gauss's Law. However, as Coulomb's force ( $\mathbf{F}_{el}$ ) on charge  $q_1$

is square dependent of the distance from the secondary charge  $q_2$  at the respective locations  $\mathbf{r}_1$ ,  $\mathbf{r}_2$ . (Eq. 1.25) This, and the fact that the surface net charge in a buffer solution is insignificant, lead to the assumption that  $\mathbf{F}_{el}$  plays a minor role in this force equilibrium.

$$\mathbf{F}_{el} = \frac{q_1 q_2}{4\pi\epsilon_0} \frac{\mathbf{r}_1 - \mathbf{r}_2}{|\mathbf{r}_1 - \mathbf{r}_2|^3} \quad 1.25$$

### Magnus Lift Force

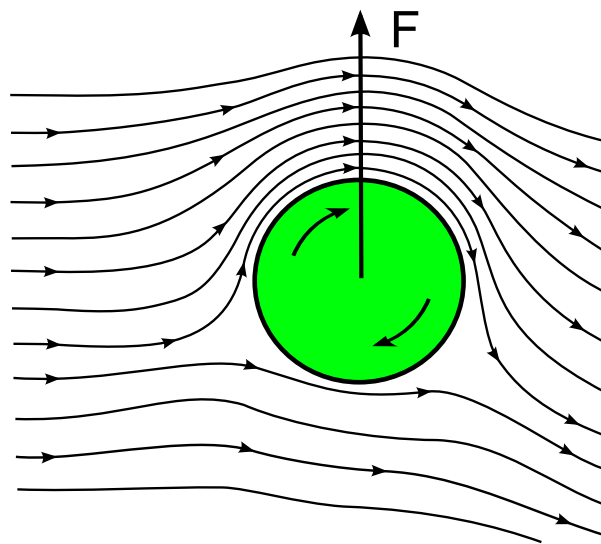


**Figure 3: Magnus Effect on a Particle in Laminar Flow**

The intrinsic rotation of a particle inside a laminar flow field causes a pressure gradient to the side whose tangential rotation vector is parallel to the stream lines.

The Magnus lift force ( $\mathbf{F}_{magnus}$ ) is a rotation-induced variable as a result of the pressure difference induced by streamline asymmetry.[16] For a spinning particle in a fluid as shown in Fig. 3, the streamline density and therefore the pressure on the one side of the particle is lower relative to the other side. The main driver of this effect is again the no-slip boundary, where fluid on the front side of the particle is dragged down whereas the fluid on the bottom side is slowed down. As a result, this leads to a lift force perpendicular to the flow direction.

$$\mathbf{F}_{magnus} = \frac{1}{8}\pi r^3 \rho_{fluid} (\mathbf{u} \times \boldsymbol{\Omega}) \quad 1.26$$

### Saffman Lift Force

When the rotation speed of a particle in shear rate direction is much greater,  $\Omega > 12\nabla\mathbf{u}$ , for a freely rotating particle Saffman lift force ( $\mathbf{F}_{\text{saffman}}$ ) will begin to act. Depending on the interaction of slip velocity and shear, it will counteract any movement to the planar surface. Hence, at high gradients the center of rotation causes a shift to the maximum shear.

Scaling with  $\omega$ , it will generally be at least one order of magnitude larger than Magnus force. Especially for electrically or magnetically actuated particles, shear-induced lift force ( $\mathbf{F}_{\text{shear}}$ ) is more relevant in the case of non-neutrally buoyant spheres.[16]

$$\mathbf{F}_{\text{saffman}} = \frac{81.2}{4}(\mathbf{u} - u_p)r^2 \sqrt{\frac{\rho_{\text{fluid}}}{\eta} \nabla \mathbf{u}} \quad 1.27$$

### Shear-induced Lift Force

This  $\mathbf{F}_{\text{shear}}$  particles to migrate toward walls until the wall lift force repels and balances it. In contrast, if the curvature of  $\mathbf{u}$  is zero, it collapses to a simple shear flow. Then the pressure will be higher on the far from the center pushing particles to the centerline of channel. As shown in Fig. 1e the magnitude of  $\mathbf{u}$  in particle is much higher on the top side of particle than that on the bottom side, due to the parabolic nature of velocity profile. Similar to Saffman force, the dissymmetry of relative velocity causes a lower pressure on the wall side, generating a shear gradient lift force which is opposite to the Saffman force.[16]

$$\mathbf{F}_{\text{shear}} = K\rho_{\text{fluid}}(\nabla \mathbf{u})^2 r^4, \text{ with } K \text{ from Eq. 1.17} \quad 1.28$$

### Deformability-Induced Lift Force

Although solidity can assumed in the first order to the study of hydrodynamic behaviour of particles in a microchannel, cells and vesicles are not rigid but deformable. The deformability will induce an additional lift forces on the particles, which is perpendicular to the main streamline, and it is subjected nonlinearities caused by the matching of velocities and stresses at the deformable particle interface.

$$\mathbf{F}_{deformation} = \mu Ur \left(\frac{r}{H}\right)^2 \frac{l_w}{H} f(\lambda) \quad 1.29$$

$$f(\lambda) = \frac{16\pi}{(\lambda+1)^3} \left[ \frac{11\lambda+10}{140} (3\lambda^3 - \lambda + 8) + \frac{3}{14} \frac{19\lambda+16}{3\lambda+2} (2\lambda^2 - \lambda - 1) \right] \quad 1.30$$

For example, deformability-induced lift force has been used already to separate and enrich malaria-infected red blood cell (RBC) from normal healthy RBC for the diagnosis of malaria. The parasite releases proteins that trigger the cross-linking of the spectrin network of the membrane, thus increases the rigidity of the infected cells.[17] Mach and Di Carlo [18] reported a parallelized microfluidic device that passively separates pathogenic bacteria from the diluted blood by the use a unique differential transit time due to channel height differences which in turn caused size-dependent inertial lift forces to obtain cell separation.

### **Fåræus and Fåræus-Lindquist Effect**

Often confused, the Fåræus and Fåræus-Lindquist effect constitute two different hemodynamic properties relevant for microfluidics with blood samples. Whereas the Fåræus effect states that RBCs are depleted in the wall regions of capillaries (due to the lift forces mentioned before), the Fåræus-Lindqvist effect describes the behavior of blood to decrease its viscosity in narrow channels.[19, 20] Thereby, the latter effect is not solely driven by the first, but also the Segré-Silberberg effect, who discovered that for neutrally buoyant particles an equilibrium at exact  $0.6r$  from a tubing center forms.[21] To model this effect, Chebbi [22] developed a cell-free marginal layer model.

#### **1.1.4. Rolling Motion and Surface Interaction of Beads**

A nice intro goes here

#### **Contact Area of a Sphere and Flat Surface**

Once the acting forces brought the bead in contact with a wall or the channel bottom, it starts to move forward in a rolling motion. In a simple model, rolling on a plane without slipping is constrained by a sphere's translation ( $\mathbf{F}_{||}$ ,  $\mathbf{F}_{\perp}$ ), rotation ( $\omega$ ), and shear. Nevertheless, due to the rigid nature of the sphere, any shear will be omitted in further models.[23] The no-slip boundary condition has to be applied also here by the require-

ment that the points of the sphere momentarily in contact with the plane are at rest. However, rolling contact problems are dynamic because the contacting bodies are continuously moving with respect to each other. The contact patch in a sliding problem continuously consists of the same particles. In contrast, particles enter and leave the contact area during rolling. Moreover, in a sliding problem the surface particles in the contact patch are all subjected the same tangential shift everywhere, whereas in a rolling problem the surface particles are stressed in different ways. During rolling, they are free of stress when entering the contact, then stick to a particle of the opposing surface, and are strained by the overall motion difference between the two bodies, until the local traction bound is exceeded and local slip sets in.[24]

In a real world, pressing two bodies with rough surfaces against each other limits the contact between the two bodies to a value, which is much smaller than the nominal contact area. Additionally, on natural and engineering surfaces Lennard-Jones potential, wetting, and molecular interactions start to play a role on the spectated microscale.[25]

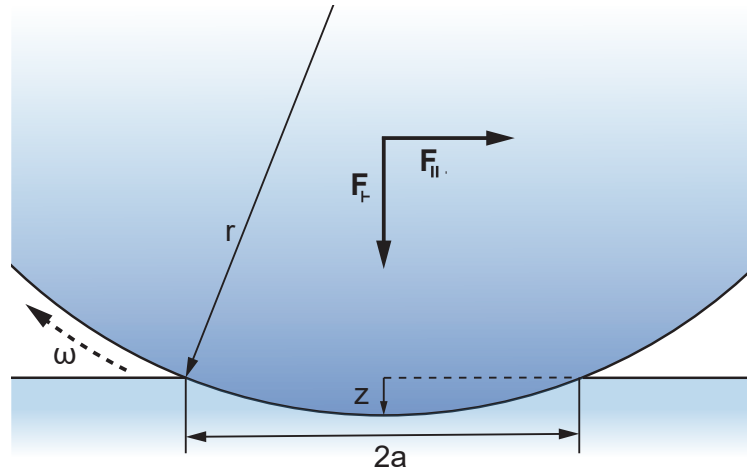


**Figure 4: Rolling Mechanics of a Sphere**

Penetration model of a sphere with radius  $r$  adapted from Azad and Featherstone [25] and Waters and Guduru [26]. The top body moves into the elastic bottom body for an approach ( $z$ ) and a contact area  $\pi a^2$ .

In reality, with elastic effects taken into consideration, a different situation occurs. If an elastic sphere is pressed onto an elastic plane (ideally of the same material), both bodies deform and a Hertzian pressure distribution arises. The center of the sphere is moved down by an approach ( $z$ ) as shown in Fig. 4 that can also be described as “maximum penetration distance”. It can now be calculated that the normal contact area between the bodies follows  $A_{contact} = \pi a^2 = \pi (2rz - z^2) = 2\pi rz \left(1 - \frac{z}{2r}\right)$ . Assuming

that  $z \ll 2r$  and considering that  $A_{contact}$  must be zero for all  $z < 0$ , the following equation for the contact area arises. (Eq. 1.31) The spherical contact surface can be calculated analogous Eq. 1.32.[25]

$$A_{contact} = 2\pi r z, \text{ for } z \geq 0 \quad 1.31$$

$$S_{contact} = \pi r(2z + a^2) = \pi z(4r - z), \text{ for } z \geq 0 \quad 1.32$$

For a  $8\mu\text{m}$  microbead and a penetration depth  $z$  of  $100\text{ nm}$  this yields for example an interaction with  $6.84\%$  of the total sphere and a total area of  $13.753\mu\text{m}$ . Several methods and experiments have already been developed in the literature to measure the resulting friction and penetration parameters. A general model of a sphere in contact with a wall was optimized by Krishnan and Leighton [27]. Experimentally, Waters and Guduru [26] developed a microtribometer in PDMS to evaluate adhesion properties and validate their model's predictions.

### **Protein interaction during Rolling**

In the attempt to mimic rolling adhesion on vascular surfaces which is the first step in recruiting circulating leukocytes and other cells into the tissue, protein-protein-interactions as driver for microbead motions have been studied extensively in this thesis. Statistically, a cell flowing near the vessel wall is able to attach if its adhesion receptors contact ligands on the wall. Bond formation, anyhow, involves distinct steps: transport, which brings two molecules into close proximity, and reaction, during which the molecules dock. Faster cell velocity produces more collisions but also limits the interaction time between interaction molecules. Thus, the relative timescales for transport and docking affect the efficiency of tethering a flowing cell to the surface.[28]

For these properties, Dembo et al. [29] developed a detailed physical description of membrane adhesion and detachment kinetics. Wu and Voldman [9] then proposed an integrated model for bead based rolling mechanisms under the influence of protein interaction. The key for interaction thereby is the specific *affinity* respectively *avidity* of the protein and its ligand. In general, high-affinity ligand binding results from greater attractive ligand-receptor-forces and results in a higher tenancy of the receptor. However,

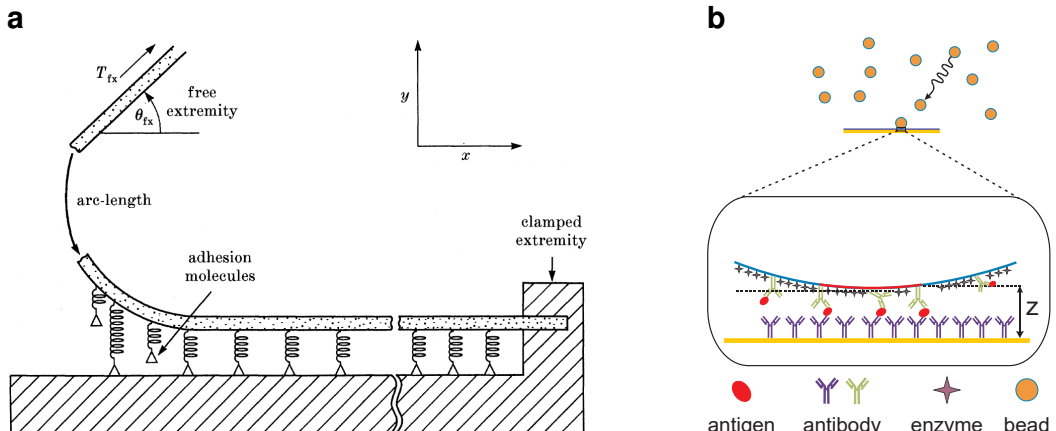


**Figure 5: Membrane Adhesion and Detachment Models**

**a** Adhesion Model after Dembo et al. [29]: Every interaction is viewed as spring-damper-model in superposition. **b** Surface Coverage Assay Model: In a stochastic approach, analyte molecules and their interactions are modeled between a planar and a spherical surface. Adapted from Wu and Voldman [9]

lifetime of a formed complex does not correlate. The net ligand affinities are unitized by the dissociation constant ( $K_d$ ), which relates the reverse reaction rate ("the dissociation of the bond") to the forward reaction rate ("the formation of the bond"). Therefore high-affinity results in low  $K_d$ .

On a bead and microchannel surface, however, not only one but multiple protein-ligand complexes are formed and dissociated simultaneously. This is described by *avidity*. Through single binding events elevate the likelihood of other interactions, avidity is not relating the sum of its ingredient affinities but can rather be seen as the combined effect of all affinities participating in the biomolecular interaction.[30]

Main factor for the method in this thesis is now the critical tension ( $T_{crit}$ ). A particle - cell or bead - flowing in a low-Reynolds number environment, experiences a  $F_{shear}$  and a torque rotation vector ( $\Omega$ ), which both reach maximum when the particle stops. For this, the two forces must be counteracted by a tensile force on the adhesive bonds and a compressive force at the bottom of the particle. Moreover, these forces affect the forward and reverse reaction rates of the bonds. Any rolling motion stops when the adhesion can withstand the force required to counteract the maximal other forces. After break-up of these bonds the particle begins to accelerate downstream until a newly formed bond develops sufficient strength. Consequently, the intrinsic mechanics of these bonds and how their respective off-rates act under force critically determines whether and how bead roll in a flow field.[28]

There exist two distinct bond types that take effect during the above processes: *Slip*

*bonds* are linkages whose lifetime is shortened to some extent by external force whereas *catch bonds* lock more tightly upon deformation stress.

In biological systems, for example selectines, another effect arises. Upon increasing external stress, bond lifetimes with the ligand are first prolonged until a threshold where bonds are starting to decease. In contrast, if an antibody is the ligand only slip bonds are formed in response to force.[31, 32] By studying the exact forces acting on a particle-protein interaction system affinity based sorting and ultrasensitive assays can be established.[33]

## 1.2. Surface Chemistry

Introducing biological samples, such as peripheral whole blood and -plasma, into microsystems needs careful consideration of surface modification compared to buffered samples of adjusted pH containing cells or polymeric beads. Blood-material contact most often initiates surface-mediated reactions that lead to cell activation, blood clotting or biofilm formation.[34, 35] In order to minimize unspecific interactions on surfaces, most contact faces are passivated with chemically and biologically inert materials or even composed entirely from it. In any use case, where a surface has to be functionalized with biomolecules, the intrinsic inertness then requires specialized methods for permanent and reproducible adhesion.[36, 37]

Molecules can be immobilized through various mechanisms on surfaces to achieve a biological or chemical functionality. The most simple is physisorption. Here, a biomolecule is bonded only by weak electrostatic, van-der-Waals or dipole-dipole interaction with a adsorption enthalpy below  $50 \text{ kJ mol}^{-1}$ .[37] In contrast, this yields fast reaction rates, because no activation energy has to be overcome. Although a large number of molecules can be captured with this method, several drawbacks have been identified.[38–41] Therefore, most functionalization approaches rely on chemisorption where molecules are covalently bound to a surface. Due to the higher activation energy barrier this bonding mechanism works slower in comparison to physisorption, though higher temperatures or catalysts can promote an equilibrium. One of the most well-known strategies to bring reproducible thin films on surfaces is the formation of self-assembled monolayers (SAMs) where a dense layer of single molecules with high internal order forms upon dipping into a surface-active substance.[42]

### 1.2.1. Surface Oxidation Methods

Modifying a surface with functional silanes, requires oxidized sites, for example  $-\text{OH}$  (hydroxyl) resp.  $\text{Si}-\text{OH}$  (silanol) groups. In order to increase the presence of those reactive groups on substrates, various activation methods such as a mixture from hydrogen peroxide with excess of sulfuric acid (piranha) and sulfuric acid ( $\text{H}_2\text{SO}_4$ ), oxygen gas ( $\text{O}_2$ ) - plasma treatment or an hydrofluoric acid (HF) dip can be chosen.[43]

Critical for any surface engineering is the internal structure and in consequence the binding energies of the surficial groups. The three mainly used substrates in this work,

glass, poly(dimethylsiloxane) (PDMS) and silicon nitride ( $\text{Si}_3\text{N}_4$ ), contain highly conserved, homogeneous surfaces and are mostly well characterized. The surface of glass exhibits already silanol groups intrinsically and consequentially demands only a removal of impurities. PDMS and  $\text{Si}_3\text{N}_4$  however have different compositions as shown in Fig. 6 and ?? hence requiring a strong oxidation agents to completely exchange its interface to hydroxyl.[44–46]

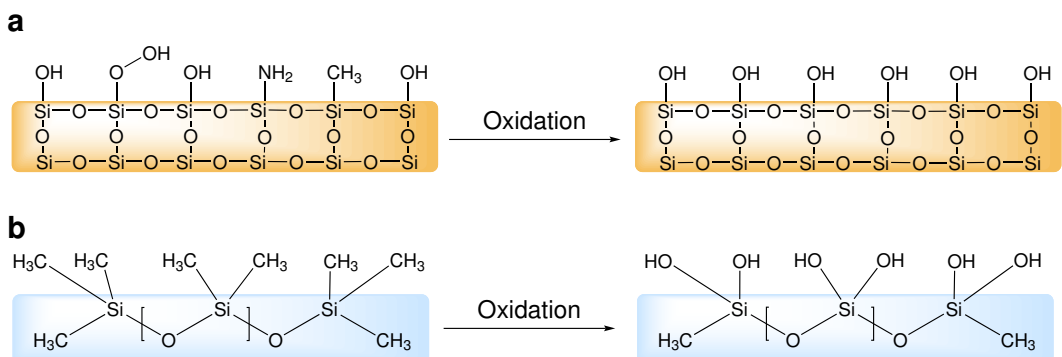
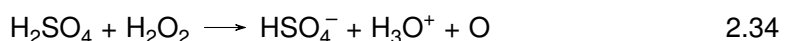
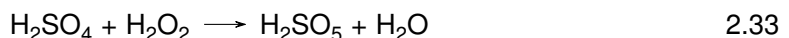


**Figure 6: Different Substrate Surfaces: Glass, PDMS and  $\text{Si}_3\text{N}_4$**

Surface groups and internal structure of quartz glass (a), PDMS (b), and silicon nitride (c). After an oxidation step, the methyl groups are converted to hydroxyl.

### Piranha Solution

Piranha is an oxidizer composed of hydrogen peroxide ( $\text{H}_2\text{O}_2$ ) and  $\text{H}_2\text{SO}_4$ , typically in volume ratios between 1:3 and 1:7. The effectiveness of piranha in removing organic residues and creating hydroxyl groups is induced by two distinct processes. First, hydrogen and oxygen are removed as units of water by the concentrated  $\text{H}_2\text{SO}_4$  in a comparably fast process.( Eq. 2.33) This occurs due to the thermodynamically favorable reaction with an enthalpy of  $-880 \text{ kJ mol}^{-1}$  and produces Caro's acid ( $\text{H}_2\text{SO}_5$ ), one of the strongest oxidants known.[47]



Second, the sulfuric acid boosts hydrogen peroxide from a mild oxidizer into the more aggressive atomic oxygen by the dehydration of  $\text{H}_2\text{O}_2$ . (Eq. 2.34) These two dehy-

dration processes result on the one hand in a highly corrosive nature against organic materials, particularly against the difficult to remove carbon. On the other hand, it is strongly acidic and oxidizing.

### **Hydrofluoric Acid**

One of the substrates used in this work is  $\text{Si}_3\text{N}_4$  as passivation layer above magnetic sensors as it has a significant better diffusion barrier against water or sodium ions and is chemically inert.[48] However, due to its complex crystal structure it is also difficult to modify by common chemicals and the exact surface composition still subject to scientific discussion.[49] Apart from cleaning the surface with piranha, few other modification methods have been reported, but only one suitable for the direct generation of hydroxyl groups.[42, 49–51]

As depicted in Fig. 6, the reaction  $\text{Si}-\text{OH} + \text{HF} \leftrightarrow \text{Si}-\text{F} + \text{H}_2\text{O}$  takes place reversibly due to the coincidence that  $\text{Si}-\text{O}$  and  $\text{O}-\text{H}$  as well as  $\text{Si}-\text{F}$  and  $\text{H}-\text{F}$  bonds have similar binding energies. Hence, the forward and reverse reactions require a low activation energy. After Le Chatelier's principle, a depletion of HF in the bulk leads then to an increase in surficial hydroxyl groups.[52] It was revealed that an oxidation with a similar protocol based on aqueous HF yields a variable  $\text{Si}-\text{O}-\text{Si}$  (siloxane) coverage with  $37 \pm 17\%$  of a monolayer, which can be used for stable, covalent attachment of silanes. Nominally, the same surface coverages of silicon oxide and nitride surfaces could be achieved by ethoxy- and chlorosilanization.[53] As shown by Gustavsson et al. [54], the subsequent surfaces exhibit beneficial biological properties and can be modified by further standard procedures.

### **Oxygen Plasma**

Apart from wet chemistry methods, the exposure of a surface to oxygen plasma yields hydroxyl groups as well. In a plasma chamber, a low-pressure gas is irradiated by kHz to MHz waves to excite and ionize its atoms. In consequence, the UV-radiation emitted by the gas can photolyse typical organic bonds and remove surface contaminations. Additionally, reactive oxygen species such as  $\text{O}_2^+$ ,  $\text{O}_2^-$ ,  $\text{O}_3$  or  $\text{O}$  oxidize the surface or bind dissociated components with low vapor pressure. During an evacuation in the process, these molecules are removed from the chamber intrinsically.[55]

### 1.2.2. Silane Chemistry

By the use of silane chemistry a surface is rendered organofunctional with alkoxy silane molecules. Since glass, silicon, alumina, titania, and quartz surfaces, as well as other metal oxide interfaces, are rich in hydroxyl groups, silanes are particularly useful for modifying these materials.[56]

The general formula for a silane coupling agent (Fig. 7a) typically shows the two classes of functionality. X is a hydrolyzable group typically alkoxy, acyloxy, halogen or amine. Following hydrolysis, a reactive silanol group is formed, which can condense with other silanol groups to form siloxane linkages. (Fig. 7) Stable condensation products are also formed with other oxides such as those of aluminum, zirconium, tin, titanium, and nickel. Less stable bonds are formed with oxides of boron, iron, and carbon, whereas alkali metal oxides and carbonates do not form stable bonds with siloxanes at all. The R group (Fig. 7a) is a nonhydrolyzable organic radical that may possess a functionality that imparts desired characteristics. One of the more common silanes is 3-triethoxysilyl-propan-1-amine (APTES), where the X group consists of an  $-\text{O}-\text{CH}_2-\text{CH}_3$  (ethoxy) group, the organic rest R is substituted by an  $-\text{NH}_2$  (amine) and the 3  $-\text{CH}_2-$  (methylene) groups alter n to 3.[57]

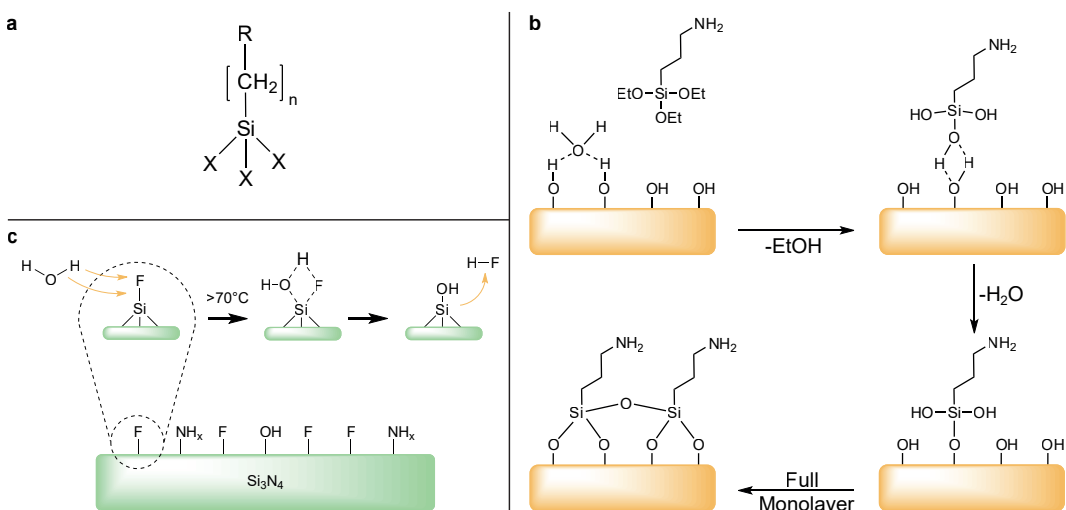


**Figure 7: Surface Oxidation and Modification by APTES**

(a) Structure of a typical trialkoxysilane, X: hydrolyzable group, R: non-hydrolyzable organic radical, n: methylene chain-length. (b) Before the condensation reaction, the oxidized surface has formed hydrogen bonds with water molecules while the silane molecules are in the bulk solution. The hydrolyzed silanol group adsorbs onto the surface and forms hydrogen bridges with the silicon bound oxygen atom. In a condensation reaction, under the loss of water, a covalent bond to the surface forms. After the SAM assembly the surface is saturated with a covalent-bound, crosslinked silane film.[58] (c) Proposed oxidation of  $\text{Si}_3\text{N}_4$  with  $\text{HF}$ : Due to similar activation energies water can displace  $\text{HF}$  in a competitive manner effectively above a temperature above  $70^\circ\text{C}$ .

The final result of reacting an organosilane with a substrate ranges from altering the adhesion characteristics, catalyzing chemical transformation at the heterogeneous interface, ordering the interfacial region, and modifying its partition characteristics. Significantly, it includes the ability to effect a covalent bond between organic and inorganic materials. Especially in optical or biological sensors, silane modifications open a broad range of applications.[42, 59, 60]

However, the silanization reactions bear a few drawbacks which are often neglected. For instance, silane chemistry is strongly temperature and pH-dependent.[61, 62] Further, in a process to build SAMs from APTES, the reaction must be catalyzed by water. But already small changes in the water content cause dramatic deviations in layer thickness.[63] Additionally, silanes can crosslink to themselves through side reactions. (Fig. 7b) [64]

### **1.2.3. Carbodiimide Crosslinker Chemistry**

By APTES amine-terminated films form the basis of many reactions and open the possibility to various applications, such as the direct attachment of biofunctional molecules by carbodiimide crosslinking chemistry.[65] Here,  $-COOH$  (carboxyl) groups are modified by 3-(Ethyliminomethyleneamino)-N,N-dimethylpropan-1-amine (EDC) and 1-Hydroxy-2,5-pyrrolidinedione (NHS) to form a stable secondary  $R_1-CONH-R_2$  (carboxamide) bond with any primary amine.

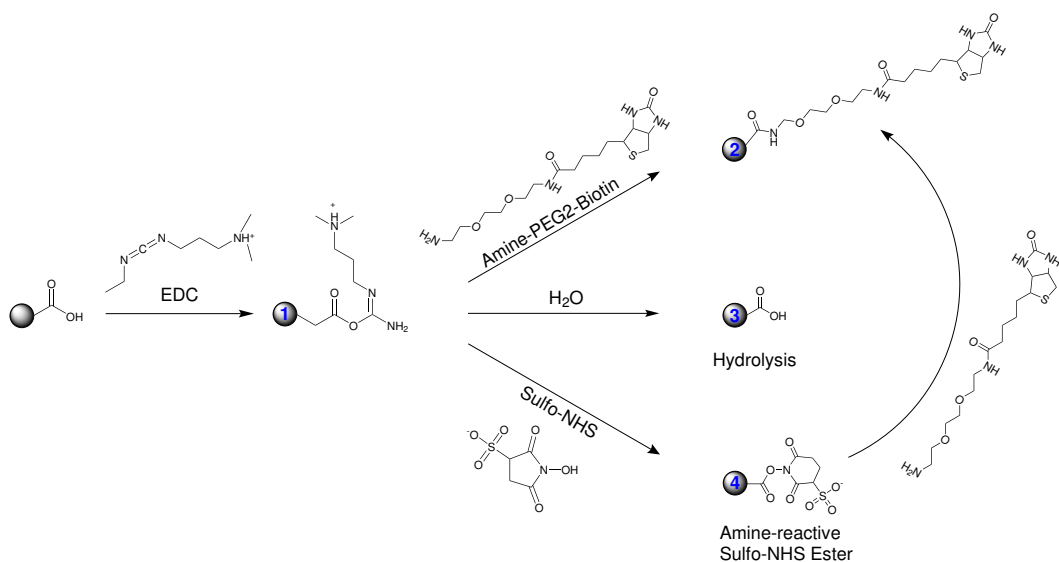


**Figure 8: Carboxyl bead modification with EDC/NHS**

The carboxyl groups on the bead are activated with EDC to an active O-acylisourea intermediate. This can then either be nucleophilically attacked by a primary amine of the amine-PEG<sub>2</sub>-biotin reactant or - due to its instability - hydrolyzed back to a regenerated carboxyl surface. A present NHS-ester can also displace the O-acylisourea to form a considerably more stable intermediate which then itself reacts with any primary amine.

The general reaction mechanism is depicted in Fig. 8 for the example of a particle surface, but it can equivalently be applied to any other modified surface or molecule. The initial carboxyl group is esterified by EDC to an active o-acylisourea intermediate and leaves rapidly upon nucleophilic attack of an amine with release of an iso-urea byproduct. A zero-length amide linkage is formed. (Fig. 8, 1->2) Sulphydryl and hydroxyl groups also will react with such active esters, but the products of such reactions, thioesters and esters, are relatively unstable compared to an carboxamide bond. (Fig. 8, 1)[65]

However, this reactive complex is slow to react with amines and can hydrolyze in aqueous solutions. If the target amine does not find the active carboxyl before it hydrolyzes (Fig. 8, 3), the desired coupling cannot occur. This is especially a problem when the target molecule is in low concentration compared to water, as in the case of protein molecules. Notwithstanding, forming a NHS ester intermediate from the reaction of the hydroxyl group on NHS with the EDC active-ester complex increases the resultant amide bond formation remarkably. (Fig. 8, 4->2) [66]

Another critical point in carbodiimide chemistry is the solubility of the compounds. EDC, NHS and 1-hydroxy-2,5-dioxopyrrolidine-3-sulfonate (sulfo-NHS) are soluble in aqueous and organic solvents. Nevertheless, activation with non-sulfonate NHS decreases water-solubility of the modified carboxylate molecule, while activation with sulfo-NHS preserves or increases its water-solubility by virtue of the charged sulfonate group.[67]

#### 1.2.4. The Biotin-Avidin-System

Until now, the interaction of the homotetrameric protein avidin and its ligand biotin forms one of the strongest known non-covalent bonds in biological systems characterized by a  $K_d$  in the range of  $10^{-15}$  M.[68] First isolated from chicken egg white, it became a standard to use in biotechnology when researchers found a similar bacteria protein - streptavidin - in *Streptomyces* strains.[69] However, the charged glycoprotein avidin exhibits unspecific binding in some assays in comparison to streptavidin. Therefor, several companies developed deglycosylated forms of avidin with a neutral isoelectric points to minimize unspecificity. (NeutrAvidin, Extravidin, NeutraLite) In recent studies, a mutant streptavidin called "Traptavidin" exhibited an even 10 times dissociation rate.[70] As discovered in the early 1990s, biotin is bound inside a highly stable  $\beta$ -barrel structure, and stabilized by hydrogen bonds and van der Waals forces.[71] In a unique mechanism, a side group of biotin (valerate) binds to a neighboring monomer of streptavidin and therefor stabilizes the dimer complex intrinsically.[72, 73] From a thermodynamical point-of-view, the interaction of the vitamin and protein is described by a total free binding energy of  $300 \text{ kJ mol}^{-1}$  to  $330 \text{ kJ mol}^{-1}$  for a tetrameric protein.[73] All these aspects lead to a significant rupture force for the biotin-release of  $250 \text{ pN}$ .[74]

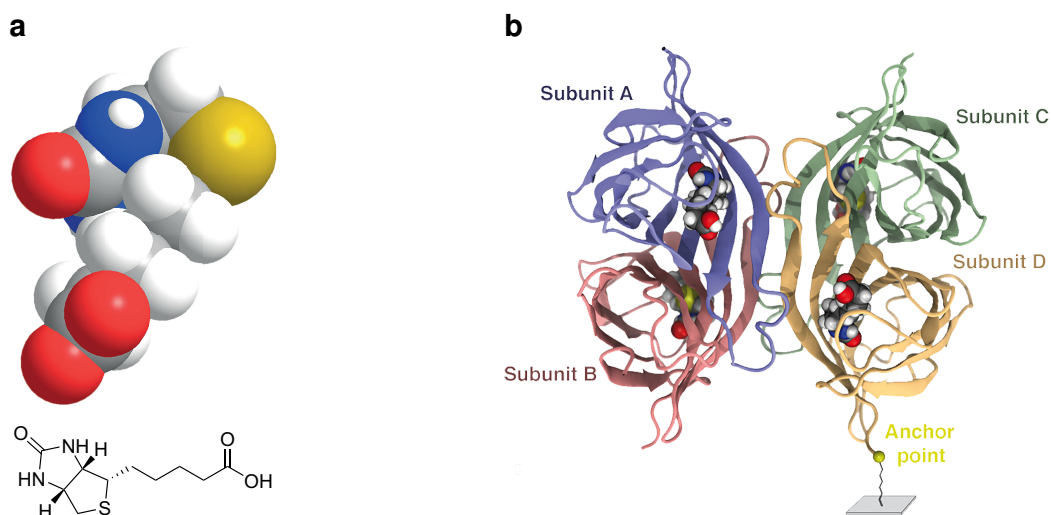


**Figure 9: Functional Structures of Biotin and Streptavidin**

(a) Two- and three dimensional chemical structure of the biotin molecule. (b) Homotetrameric streptavidin with four subunits and four bound biotin-ligands. The molecule is attached with the anchor point at one terminus to a surface.[75]

### 1.3. Magnetoresistive Sensing

The measurement system's main component is a GMR-sensor stack with a measured magnetoresistive effect of ~8 %. GMR is a quantum mechanical magnetoresistance effect observed in multilayers composed of alternating ferromagnetic and non-magnetic conductive layers. The driving factor for this resistance is anisotropy of a soft ferromagnetic layer. Two ferromagnetic layers with a thin conducting, non-magnetic spacer in the center build the base of the GMR stack.[76] One ferromagnetic layer has a so called pinned magnetization by exchange coupling, which is insensitive to outer magnetic fields. The second, "easy" layer is soft magnetic. Hence, it modulates its orientation in dependence to small coercive forces. [77]

In the case if both layers are aligned parallel, applying a current to the sensor allows majority charge carriers to pass through the layers with less impact into electrons on either sides. Accordingly, the overall resistance is low compared to another extremum in the antiparallel alignment. The magnetization direction can be controlled, for example, by applying an external magnetic field.[78, 79]

In the present system, GMR stacks were used in a Wheatstone configuration, where two bridges act as a reference for bridge balancing. In front of the sensor, nickel-based chevron patterns act as pre-enrichment for magnetic particles. These structures are driven by an external permanent magnet hence imposing a high flux density gradient on particles. Above these patterns, previously mentioned  $\text{Si}_3\text{N}_4$  passivation has been deposited in various thicknesses to achieve inertness. On top of the sensor chip, a straight microfluidic channel is mounted to execute flow cytometry experiments.[80, 81]

In order to measure the change in resistance sensitively, the lock-in principle is used. Here, an amplifier extracts signals in a defined frequency band around a reference frequency. This efficiently filters all other frequency components. Thereby a lock-in amplifier performs a multiplication of its input  $V_s(t)$  with a reference signal  $V_r(t)$  and low-pass filters the result  $Z(t)$ . In most integrated cases, the reference signal is generated additionally by the lock-in amplifier itself. Using a pure sine wave as reference enables a selective measurement at the fundamental frequency or its harmonics.[82]

At a measurement,  $V_s(t)$  is split and separately multiplied with the reference signal and

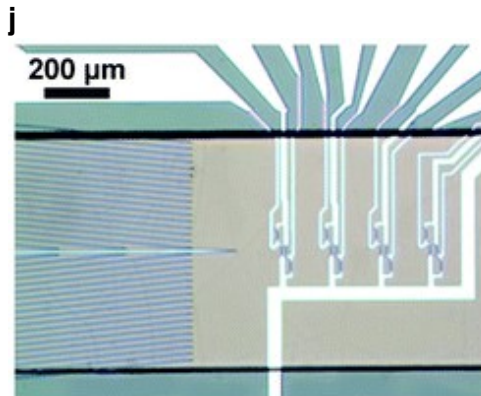
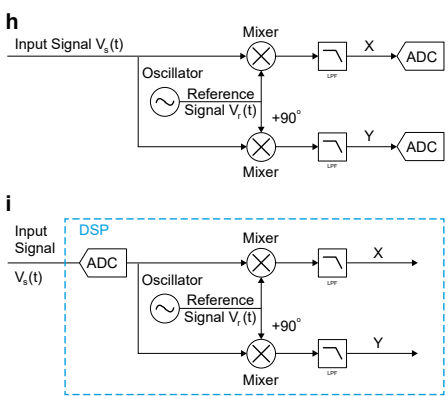
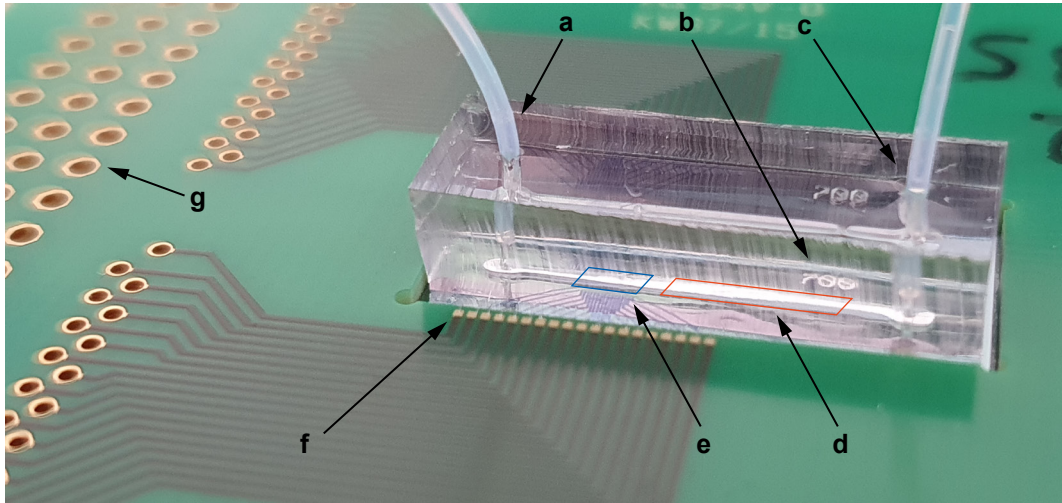


**Figure 10: Overview over the MRCyte Sensor Setup**

(a) Microfluidic outlet connection to waste reservoir. (b) Imprinted channel width. (c) Microfluidic inlet connection to syringe pump. (d) Magnetophoretic focusing region, not visible in this picture. (e) GMR-sensor region, the supply and bridge balancing traces are visible. (f) Gold bondpad: In order to connect the silicon sensor chip with the breakout printed circuit board (PCB), wedge bonds from the chip pads to the PCB pads are forged. (g) Through hole plating for the connection to the lock-in via jumper cables or a soldered connector plug. (h) Typical signal processing flow of a lock-in. The reference signal  $V_r(t)$  is splitted and mixed with the input signal with a phase difference of  $0^\circ$  and  $90^\circ$ . Then, both signals are low-pass filtered and sampled by an analog-to-digital converter (ADC). (i) Accordingly, in a digital signal processing (DSP) device the input signal is digitally converted beforehand, which in turn requires a highly sensitive and fast ADC. In contrast, DSP is more accurate and allows for software-controllable technical opportunities. (j) GMR-sensor bridge circuit inside the microfluidic channel. On the left hand side, magnetophoretic focusing structures are visible. On the right hand side, four Wheatstone bridges on a compliant ground plane can be observed.

a  $90^\circ$  phase-shifted copy of it. After demodulation, the result is constituted from signal components at the sum and the difference of signal and the reference frequency,  $\omega_s$  and  $\omega_r$ , respectively.(Eqs. 3.35 to 3.37) In the resulting signal, the trigonometric functions are Euler transformed and the magnitude  $R = \sqrt{X(t)^2 + Y(t)^2}$  acts as measurand. The high frequency compounds are then filtered digitally by a low-pass filter of varying order  $n$  to increase signal-to-noise ratio (SNR). As described in Eq. 3.39, a low-pass in the frequency domain can be described by a power series of first-order filters.

$$V_s(t) = \sqrt{2}R \cdot \cos(\omega_s t + \Theta) \quad 3.35$$

$$V_r(t) = \sqrt{2}e^{-i\omega_r t} = \sqrt{2} \cos(\omega_r t) - i\sqrt{2} \sin(\omega_r t) \quad 3.36$$

$$Z(t) = X(t) + iY(t) = V_s(t) \cdot V_r(t) \quad 3.37$$

$$= R \left[ e^{i((\omega_z - \omega_r)t + \theta)} + e^{-i[(\omega_z + \omega_r)t + \theta]} \right] \quad 3.38$$

$$H_n(\omega) = H_1(\omega)^n = \left( \frac{1}{1 + i\omega\tau} \right)^n \quad 3.39$$

However, with this measurement principle SNR can not increase infinitely. If the signal strength cannot be increased, the noise has to be reduced or avoided as much as possible. Nevertheless, noise is always caused by different sources in analog signals, for example thermal, shot, and flicker noise. Other sources are of technical origin, as for example ground loops, crosstalk, 50 Hz noise or electromagnetic pick-up. [82]

Now, to characterize a GMR with the lock-in, the easy layer has to be deflected to the full extents. For this, Helmholtz coils impose a high field in the orthogonal direction. The lock-in captures a hysteresis during the sweep from parallel to anti-parallel alignment of the layers at a specific bridge circuit. The steepness hereby indicates the sensitivity of the sensor element in the units  $V T^{-1}$ .